A facile approach for the synthesis of porous hematite and magnetite nanoparticles through sol-gel self-combustion

Imene GRITLI[1,2,]* , Afrah BARDAOUI[1] , Jamila BEN NACEUR[1] , Salah AMMAR[1] ,
Mohammad ABU HAIJA[3] , Sherif Mohamed Abdel Salam KESHK[1] , Radhouane CHTOUROU[1]

[1]Nanomaterials and Systems for Renewable Energy Laboratory, Research and Technology Center of Energy, Technopark Borj Cedria, Hammam Lif, Tunisia
[2]Faculty of Sciences of Tunisia, University of Tunisia El Manar, El Manar, Tunisia
[3]Department of Chemistry, Khalifa University of Science and Technology, Abu Dhabi, United Arab Emirates

Abstract: Porous magnetite (Fe_3O_4) and hematite (α-Fe_2O_3) nanoparticles were prepared via the sol-gel auto-combustion method. The gels were prepared by reacting ferric nitrates (as oxidants) with starch (as fuel) at an elevated temperature of 200 °C. Different ratios (Φ) of ferric nitrates to starch were used for the synthesis (Φ = fuel/oxidant). The synthesized iron oxides were characterized by Fourier transform infrared (FT-IR) spectroscopy, Raman spectroscopy, X-ray diffraction (XRD) spectroscopy, scanning electron microscopy (SEM), transmission electron microscopy (TEM), Brunauer–Emmet–Teller (BET) and vibrating sample magnetometer (VSM) analysis techniques. The crystal structure, morphology, and specific surface area of the iron oxide nanoparticles (Fe_3O_4 and α-Fe_2O_3) were found to be dependent on the starch content. The FT-IR, XRD and VSM analysis of the iron oxides for Φ = 0.3 and 0.7 confirmed the formation of the α-Fe_2O_3 core, whereas at Φ = 1, 1.7, and 2 showed that Fe_3O_4 cores were formed with the highest saturation magnetization of 60.36 emu/g at Φ = 1. The morphology of the Fe_3O_4 nanoparticles exhibited a quasi-spherical shape, while α-Fe_2O_3 nanoparticles appeared polygonal and formed clusters. The highest specific surface area was found to be 48 m^2 g^{-1} for Φ = 1.7 owing to the rapid thermal decomposition process. Type II and type III isotherms indicated mesoporous structures.

Key words: Fe_3O_4 nanoparticles, hematite, starch, sol-gel auto combustion

1. Introduction

Nanoparticles (NPs) are at the front of quick advancement in nanotechnology. These indispensable and superior materials exhibiting elite size-subordinate properties can find their applications in various fields [1]. In general, iron oxide NPs are widespread and commonly used. They can find their applications in many biological and industrial activities [2,3]. The three most widespread forms of iron oxides in nature are magnetite (Fe_3O_4), maghemite (Φ-Fe_2O_3), and hematite (α-Fe_2O_3). Magnetic Fe_3O_4 and α-Fe_2O_3 NPs can be potentially used in the field of biomedicine as they exhibit low toxicity and superparamagnetic properties [4,5]. Fe_3O_4 exhibits a cubic inverse spinel structure and can be utilized for developing storage media and ferrofluids. They can be used for treating hyperthermia [6,7] and in the fields of drug delivery [8], biomedicine [9,10] and catalysis [11,12].

Iron oxide NPs with suitable surface properties can be prepared via several techniques such as physical, biological, and chemical procedures. The physical methods, such as pulsed laser deposition [13], are easily executed but difficult to control the nanometric size of the prepared particles and may require high temperatures [14–16]. The biological methods [17] are of low cost but relatively slow [14,16]. The chemical methods, such as coprecipitation [18–20], sol-gel synthesis [21–23], template-assisted synthesis [24], reverse micelle [25], hydrothermal [26], solvothermal [27], sonochemical [28,29], combustion synthesis [30–34], electrodeposition [35], and pyrolysis [36] are of low cost and high yield products in which size, composition and the shape of nanoparticles can be controlled [14,16]. Among these chemical methods, the coprecipitation is an easy and rapid procedure at low temperatures (<100 °C). However, the coprecipitation procedure has some restrictions as the exploit of nonenvironmental-friendly chemicals and a limit to control size and shape of final product [14,16]. The hydrothermal procedure normally produces NPs with a high crystallinity degree, but it needs higher temperatures than the coprecipitation [16]. Sol-gel self-combustion route is a fast preparation route. The advantages of this

* Correspondence: imenegritli26@gmail.com

route include the use of few precursors and the formation of nontoxic byproducts. A minimum number of preparation steps are involved, and the efficiency of the scale-up process is high. The final products can be obtained in high yields [35]. In the sol-gel method, usually referred to as the sol-gel auto combustion, sol-gel autoignition, or sol-gel self-combustion method. The nitrates of the constituent metal ions (oxidant) and a suitable organic compound (a chelating agent that ignites the reaction; fuel), such as urea, glycine, and citric acid are used as the precursors, owing to their high solubility in water.

The fuel to nitrate ratios can significantly affect the particle size and magnetic properties of the NPs. The equivalence ratio of an oxidant and fuel mixture (Φ) can be computed in terms of the elemental stoichiometric coefficient [37]. The influence of the chelating/combustion/fuel agents on the structural and magnetic properties of iron oxide has been previously reported [38,39]. The fuel/oxidant ratio (Φ) significantly affects the flame temperature and the whole burning cycle. Therefore, the particles morphology, crystalline phase, and surface area of the particles can be controlled by manipulating the combustion temperature. A group of organic compounds (e.g., citric acid, urea, glycine, oxalyl dihydrazide, carbohydrazide, tetra form triazine, N, N-diformylhydrazine, and hexamethylene tetra mine) have been used in the combustion process as high-temperature fuels [40]. Recently, the influence of citric acid, Cetyltrimethylammonium bromide (CTAB), urea, and glycine has been determined [30,34], and a single phase of Fe_3O_4 exhibiting a high specific surface area was obtained. The synthesis of hematite nanoparticles using microwave assisted sol-gel auto-combustion method using ferric nitrate as oxidizer and a mixture of urea and glycine fuel as reducer [32]. The results showed that the powders were composed of polycrystalline oxides with a crystallite size of 30 nm of gamma Fe_2O_3 phase without sintering. In addition, the electrical conductivity of nano Fe_2O_3 in pellet form increases with the increase in frequency of impedance analyzer owing to hopping of charge carriers amongst localized sites [32]. On the other hand, starch (α1,4-glucan) is one of the most widely used polysaccharides as it is widely available, biodegradable, safe, and cheap [41]. Its physicochemical properties (for example, hydrophilicity, high chemical reactivity, chirality, chelation, flexible matrix, and adsorption capacities) have helped expand the green arrangements or strong state-based planning of metal oxide NPs [33,42].

Furthermore, some improved kinds of starch produced enzymatically (porous starch) and synthetically (functionalized starch) show the option to coordinate the sizes and states of the metal oxide NPs [39,43]. The facile preparation approach for both hematite and magnetite is essential to facilitate their use in several industrial fields. Herein we report a novel sol-gel auto-combustion synthesis of porous hematite and magnetite nanoparticles in which starch has been used as single-fuel at a low temperature (200 °C) for the first time. The effects of the starch fuel composition ratio on the crystallite sizes, morphologies, and surface areas were evaluated.

2. Materials and methods

2.1. Chemicals
Ferric nitrate nonahydrate Fe $(NO_3)_3$.$9H_2O$ (404 g/mol molecular weight; ≥ 98 % purity) and ammonia solution (17.03 g/mol molecular weight; 28 % purity) were purchased from SIGMA-ALDRICH. Commercial starch powder ($C_6H_{10}O_5$)$_n$, extracted from cereal grains such as corn, was purchased from Tunisia [44].
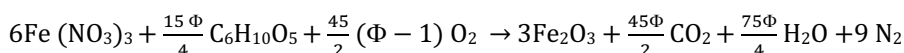
2.2. Synthesis of MNPs
The magnetic iron oxide nanoparticles (MNPs) were prepared by the sol-gel autoignition strategy utilizing Fe $(NO_3)_3$.$9H_2O$ as the oxidant and starch as the fuel. The relative fuel-to-oxidant ratio (Φ) was determined utilizing the following equation [45]:
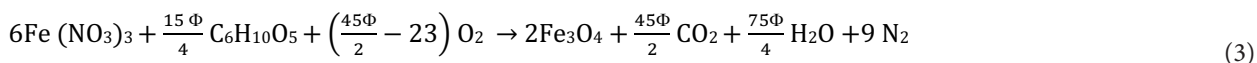
$$\Phi = \frac{n \cdot VR}{-m \cdot VO} \tag{1}$$

where n and m denote the mole fraction of the monomer of starch and ferric nitrate, respectively. VR and VO represent the total reducing and oxidizing valences of the distinctive crude material respectively. C and H atoms are considered as reducing elements with the corresponding valences of +4 and –1, whereas O is considered as an oxidizing element with the valency of –2. N is assumed to have a valency of 0. The valency of Fe is considered as +3. In this work, the reduction valence of the monomer of starch ($C_6H_{10}O_5$) is (24 + 10 – 10) = + 24, whereas the valence of the metal nitrate, Fe $(NO_3)_3$ is (3 – 18) = – 15. Here, the relative fuel-to-oxidant ratio is considered fuel-lean when Φ < 1, stoichiometric when Φ = 1, and fuel-rich when Φ > 1. On the base of the propellant chemistry [45], the redox processes occurring during the combustion process can be outlined as follows:

Fuel-lean condition:

$$6Fe\,(NO_3)_3 + \frac{15\,\Phi}{4} C_6H_{10}O_5 + \frac{45}{2}(\Phi - 1)\,O_2 \rightarrow 3Fe_2O_3 + \frac{45\Phi}{2} CO_2 + \frac{75\Phi}{4} H_2O + 9\,N_2$$

Fuel-rich condition:

$$6Fe(NO_3)_3 + \frac{15\,\Phi}{4} C_6H_{10}O_5 + \left(\frac{45\Phi}{2} - 23\right) O_2 \rightarrow 2Fe_3O_4 + \frac{45\Phi}{2} CO_2 + \frac{75\Phi}{4} H_2O + 9\,N_2 \tag{3}$$

Different molar ratios of starch (variable) to Fe $(NO_3)_3$.$9H_2O$ (constant) [$(C_6H_{10}O_5)_n$: Fe$(NO_3)_3$.$9H_2O$ = 0.2, 0.4, 0.6, 1, and 1.3] were used to study the role of starch to ferric ratio on the innovative combustion process. The ignition temperature was kept constant. The fuel-to-oxidant ratio Φ (Eq. 1) is presented in Table 1 for fuel lean ($\Phi = 0.3$ and 0.7), stoichiometric ($\Phi = 1$), and fuel rich ($\Phi = 1.7$ and 2) conditions. A typical synthesis procedure is: ferric nitrate monohydrate was dissolved in 50 mL of water followed by the addition of a specific amount of starch (Table 1). The components of the mixture were mixed for 30 min to produce a homogeneous solution. Following this, an alkali solution was added dropwise to adjust the pH to 7. Maintaining a pH during the synthesis at 7 was important to keep the stability of starch [46]. Thus, a solution with pH 7 insures a better stability of metal starch solution [47]. Subsequently, the obtained solution was mixed until a transparent sol was formed, which was dried at 95 °C over a period of 48 h. Following this, a hydrated iron gel was obtained. Combustion of the product was carried out at a temperature of 200 °C, over 1 h in a muffle furnace. Upon heating, the gel underwent a violent exothermic reaction which propagated spontaneously. This was accompanied by a release of gases. At the end of the combustion reaction, the voluminous and fragile foam was produced. After cooling the mixture to room temperature, the foam was ground using an agate mortar, and the iron oxide nanoparticles at various fuel-to-oxidant proportions ($\Phi = 0.3$, 0.7, 1, 1.7, and 2) were obtained.

2.3. Spectroscopy measurements
FT-IR spectra (KBr pellets) were recorded on a VERTEX 80 spectrometer in the range of 400–4000 cm^{-1}.

Raman spectra were recorded at room temperature using a Raman HORIBA Jobin-Yvon spectrometer: Lab Ram H and argon laser at 488 nm were used. For each sample, three distinct points were placed and measured between 100 and 800 cm^{-1}.

UV-vis spectra with diffuse reflectance spectroscopy (UV-vis DRS) were recorded with PerkinElmer Lambda 950 spectrophotometer in the wavelength range of 400−800 nm at room temperature.

2.4. X-ray diffraction (XRD)
Structural characterizations of the oxide samples were performed using the XRD Bruker Model: D8 advance X-ray diffractometer under conditions of CuKα radiation (λ= 0.15418 nm). The system was operated at 40 kV and 30 mA. Diffraction patterns were recorded in the 2θ range of 10°–70°. The crystallite size of the obtained powder was calculated from the peak of (311) using the Debye Scherrer formula [48]:

$$D = \frac{0.9 \times \lambda}{\beta \times \cos\theta} \tag{4}$$

where D represents the crystallite size in nm, λ is the radiation wavelength (λ = 0.15406 nm), β denotes the full width at half of the maximum of the diffraction lines in radians, and θ represents the Bragg-angle. In addition, structural phase and crystallite size were determined by the Rietveld refinement analysis, using FullProf program.

2.5. Field emission scanning electron microscopy (FESEM)
The surface morphologies of the synthesized powder were observed using the Philips XL30 SFEG FESEM instrument equipped with an energy-dispersive spectrometer (EDS). The chemical composition of the samples was analyzed.

2.6. High-resolution transmission electron microscopy (HRTEM)
The size distribution was evaluated by studying the TEM images recorded using the TECHNAI 20-Philips instrument (G20, 200 kV). The powders were ultrasonically dispersed in ethanol.

Table 1. Required amount of starch and ferric nitrate and their corresponding Φ.

Molar ratio	Fe $(NO_3)_3$.$9H_2O$ (g; mol)	Starch (g; mol)	Φ
0.2	2; 0.005	0.169; 0.001	0.3
0.4	2; 0.005	0.339; 0.002	0.7
0.6	2; 0.005	0.508; 0.003	1
1	2; 0.005	0.847; 0.005	1.7
1.3	2; 0.005	1.017; 0.006	2

2.7. Thermogravimetric analysis (TGA)

Thermal decomposition of the dried gel was studied using the thermogravimetric analysis and differential scanning calorimetry (TG/DSC) techniques (TA instrument; model no. 2950 New Castle, DE with a heating rate of 10 °C/min under nitrogen atmosphere).

2.8. Brunauer–Emmett–Teller (BET) surface area measurements

The porosity and the specific surface area of the oxides were determined by the BET nitrogen gas adsorption-desorption analysis conducted at 77 K using the Micromeritics ASAP 2020 instrument. The pore size distribution was evaluated using the Barrett–Joyner–Halenda (BJH) method.

2.9. Magnetic properties

The magnetic properties of the produced particles were measured by a Quantum Design PPMS magnetometer. Their isothermal 300 K dc-magnetization M was measured by cycling the magnetic field H between +70 and –70 kOe.

## 3. Results and discussion

3.1. FTIR analysis

FTIR spectral profile recorded for the prepared iron oxide NPs under conditions of $\Phi = 0.3$ and 0.7 after the calcination process at 200 °C (Figure 1) showed the absence of bands corresponding to the aliphatic groups derived from starch fuel. In the range of 800 to 400 cm^{-1}, the Fe-O vibrational bands corresponding to hematite at 450 cm^{-1} and 567 cm^{-1} were recorded (Figure 1). The bands at 567 cm^{-1} and 450 cm^{-1} can be attributed to the transverse absorption (Eu) of α-Fe$_2$O$_3$ structure [49]. This result confirms the formation of Fe$_2$O$_3$ under conditions of low fuel composition ratio. Figure 2 reveals the characteristic bands at 1632 cm^{-1} corresponding to the stretching and bending vibrations of OH adsorbed on the surface of the α-Fe$_2$O$_3$ under conditions of low calcination temperature [50]. On the other hand, the spectrum displayed the presence of a small band at 1383 cm^{-1} that can be attributed to the NO stretching band originating from the residual ferric nitrate precursor [50,51]. Figure 2 exhibits a strong absorption vibrational band attributable to Fe-O (in Fe$_3$O$_4$) at 567 cm^{-1} when $\Phi = 1$, 1.7, and 2 [20]. Furthermore, Figure 2 indicates the presence of the stretching and bending OH vibrations (originating from water; adsorbed on the surface of the formed Fe$_3$O$_4$) at approximately 3439 cm^{-1} and 1632 cm^{-1}, respectively [51]. Moreover, the FT-IR spectral profile of Fe$_3$O$_4$ NPs also revealed the presence of a small absorption band at 1381 cm^{-1}. This peak could be assigned to the NO stretching band originating the residual ferric nitrate precursor [49]. Bands corresponding to the hematite structure were not observed in the spectral profile presented in Figure 2. Therefore, the combustion synthesis process of α-Fe$_2$O$_3$ and Fe$_3$O$_4$, using starch as the fuel, is mostly influenced by the nature of the fuel used and the fuel-to-oxidant proportion (Φ).
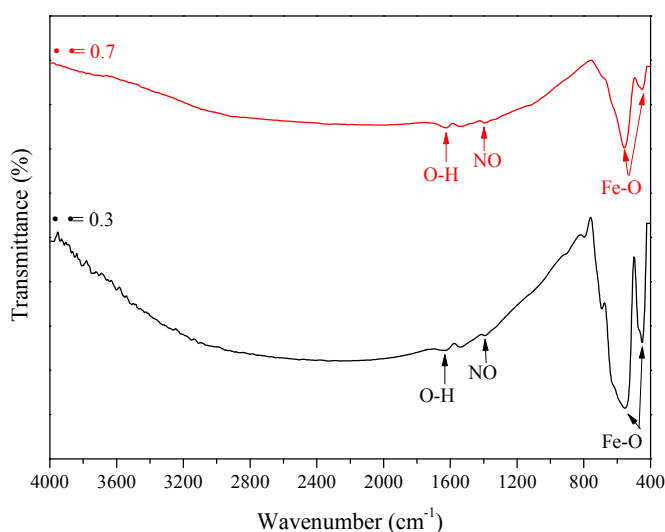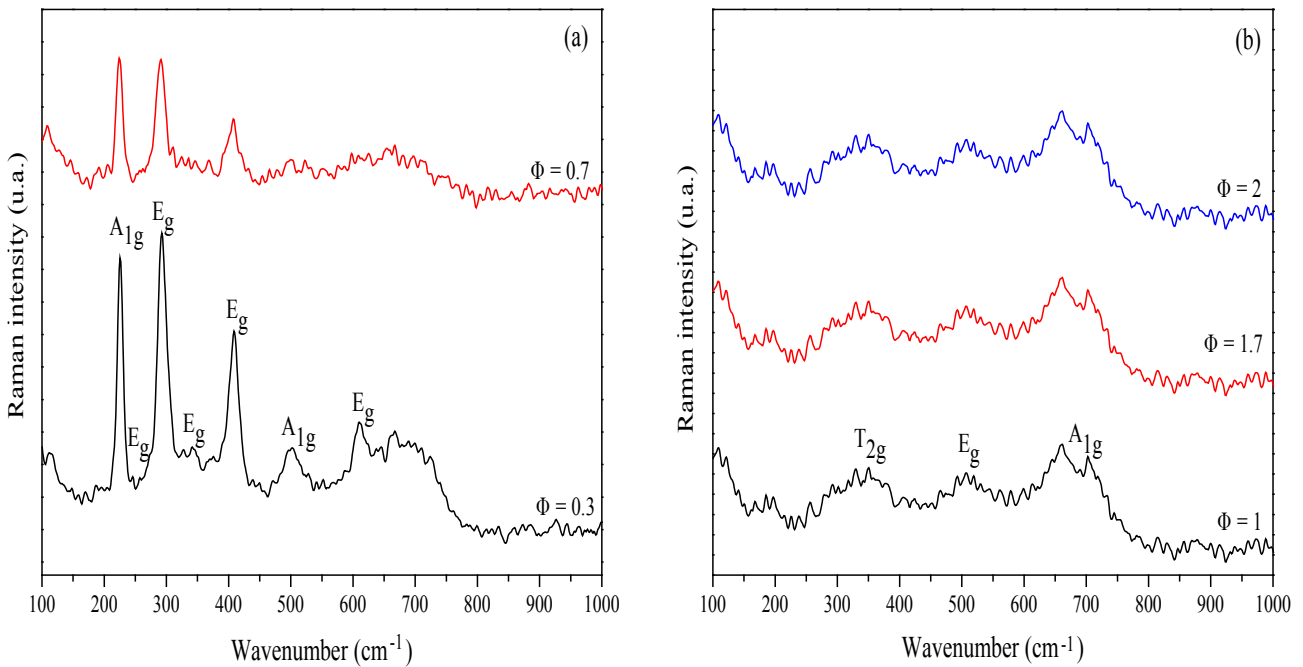

Figure 1. FTIR spectral profile of the resultant iron oxide at different starch to ferric nitrate ratios ($\Phi = 0.3$ and 0.7).

3.2. Analysis of Raman spectra

Raman spectra of the resultant iron oxides at different Φ (0.3, 0.7, 1, 1.7, and 2) were recorded using excitation lasers at 488 nm (Figure 3). Generally, hematite belongs to the R-3c crystal space group. Seven phonon mode lines are anticipated in the Raman spectrum: five E_g phonon and two A_{1g} modes [20]. E_g modes at 245, 292, 298, 411, and 611 cm^{-1} and A_{1g} modes at 225 and 496 cm^{-1}, can be observed in the spectral profile recorded under conditions of varying Φ (Φ = 0.3 and 0.7; Figure 3a). These results confirm the existence of α-Fe$_2$O$_3$ at low Φ. Similar results were obtained by analyzing the FT-IR spectral profiles. Raman spectra recorded for Φ = 1, 1.7, and 2 exhibited bands that correspond to the maghemite Φ-Fe$_2$O$_3$ (Figure 3b). The three Raman active phonon modes (T_{2g}, E_g, and A_{1g}) of maghemite appeared at 350 cm^{-1} (T_{2g}), 512 cm^{-1} (E_g) and
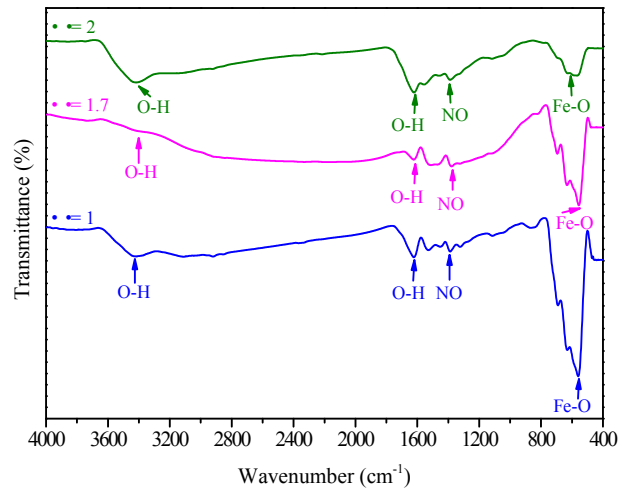
Figure 2. FTIR spectral profile of the resultant iron oxide at different starch to ferric nitrate ratios (Φ = 1, 1.7, and 2).

Figure 3. Raman spectral profiles of the resultant iron oxides at different starch to ferric nitrate ratios Φ = 0.3 and 0.7 (a); Φ = 1, 1.7, and 2 (b).

703 cm^{-1} (A$_{1g}$) (Figure 3b) [52]. This transformation to maghemite for Φ = 1, 1.7, and 2 can be potentially attributed to the oxidation of magnetite into maghemite by the heating effect of the incident laser irradiation.

3.3. Analysis of XRD patterns

Figure 4 confirmed the presence of the rhombohedral crystallographic phase of α-Fe$_2$O$_3$ at Φ = 0.3 and 0.7. Seven characteristic peaks for α-Fe$_2$O$_3$ were allocated at 2θ = 24.19°, 33.12°, 35.67°, 41.0°, 49.50°, 54.0°, and 62.45°). The peaks corresponded to the (012), (104), (110), (113), (024), (116), and (214) planes, respectively (JCPDS cards No.01–086–0550) [53]. The typical XRD pattern of the Fe$_3$O$_4$ nanoparticles was obtained at Φ = 1, 1.7, and 2 (Figure 4). The XRD patterns recorded with Fe$_3$O$_4$ revealed the presence of peaks at 30.23° (220), 35.57° (311), 37.29° (222), 43.20° (400), 53.70° (422), 57.24° (511), and 62.86° (440) (JCPDS No.01–075–0033) [31,54]. However, the intensity of the XRD peaks for Fe$_3$O$_4$ nanoparticles decrease at high Φ value that inhibit the combustion reaction due to the formation of residual carbon on the ion oxide surface [31]. Analysis of the FT-IR, Raman, and XRD spectral profiles revealed that the degree of inversion of the ferric (Fe^{3+}) and ferrous (Fe^{2+}) ion samples is affected by the fuel composition ratio. At a high starch ratio ($\Phi \geq 1$), an excessive quantity of gases, such as CO and CO$_2$, and heat are produced.

Consequently, the ferric ions (Fe^{3+}) get reduced by CO gas to form ferrous ions (Fe^{2+}) according to Equation (5). Subsequently, the magnetic phase is formed.

$$3Fe_2O_3 + CO \quad \rightarrow \quad 2Fe_3O_4 + CO_2 \tag{5}$$

Furthermore, less amount of energy is required to convert ferric nitrate to hematite than that required to convert it to magnetite.

ΔH for the formation of hematite and magnetite are –823.5 and –1121 KJ/mol, respectively based on previous reports [55].

The Rietveld refinement results of the synthesized iron oxide nanoparticles at Φ= 1 are illustrated in Figure 5. The experimental spectra are represented by circles while the full line corresponded to the calculated data. The difference between the observed and the calculated pattern are represented in the curve at the bottom. As shown in Figure 5, good agreements can be found between calculated and observable spectra indicating a high fit. The Rietveld parameters goodness of fit (χ^2), Bragg factor R$_B$ and the R$_F$ factor were estimated as 1.5; 3.14 and 3.16, respectively. The high agreement between the observed and calculated pattern affirm the formation of Fe$_3$O$_4$ phase at Φ = 1.

The estimated average crystallite size at Φ = 1 by Rietveld refinement is 37.02 nm while the one calculated using Debye Scherrer formula is 34.71 nm. The average crystallite size from Rietveld analysis is slightly higher than the calculated using Debye Scherrer. This may be due that refinement is determinate using all peaks, but for these calculated from Debye Scherrer formula only (311) peak was considered. The average crystallite obtained by Debye Scherrer formula sizes increased from 26.65 nm at Φ = 0.3 to 32.25 nm at Φ = 0.7. In addition when Φ = 1 the magnetite phase reaches a maximum level (Figure
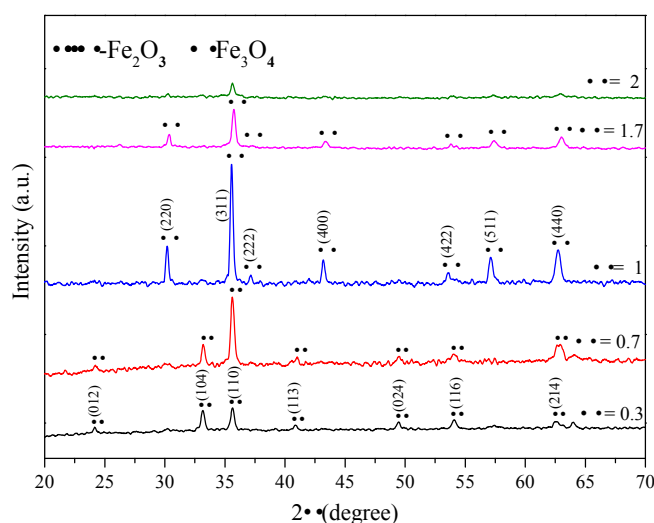
Figure 4. XRD patterns of the resultant oxides at different starch to ferric nitrate ratios (Φ = 0.3, 0.7, 1, 1.7, and 2).
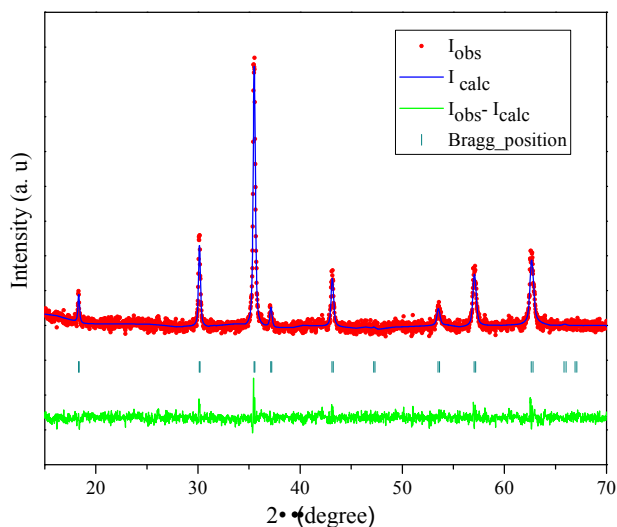
Figure 5. Rietveld refined XRD patterns for synthesized iron oxide nanoparticles at $\Phi = 1$.

4) and the crystallite size increased reaching the highest value of 34.71 nm. However, when the fuel-to-oxidant ratio increased to $\Phi = 1.7$ and 2 the crystallite size of Fe_3O_4 decreased to 31.27 nm and 25.9 nm, respectively, and fine particles were formed. This can be explained by the presence of the residual carbon owing to combustion of starch in the Fe_3O_4 nanoparticles [31].

3.4. Analysis of SEM images

The morphologies of the prepared magnetite nanoparticles at different Φ (1 to 2) were characterized by studying the FESEM images (Figure 6). These magnetite nanoparticles exhibit a quasi-spherical shape that showed excellent rates of internalization. They also exhibited the highest rate of cellular uptake owing to the presence of van der Waals forces among particles that lead to strong agglomeration (Figure 6). The α-Fe_2O_3 nanoparticles (at $\Phi = 0.3$ and 0.7) agglomerate with an overall polygonal morphology. For $\Phi = 0.3$ and $\Phi = 0.7$ (fuel-lean condition), the agglomerates imply thick slices.

However, as the amount of fuel is increased in $\Phi = 1$ (stoichiometric equilibrium), the agglomerate forms large clusters. Whereas, for $\Phi = 1.7$ and 2 the densities of the Fe_3O_4 nanoparticles decrease as the Fuel ratio increases and the dispersion of the nanoparticles improves [31].

EDX profiles were analyzed to identify the elemental composition of the samples. The EDX of $\Phi=1$ (Figure 7) shows one peak for oxygen (O) (at ≈ 0.5 KeV) and three peaks for Fe (at ≈ 0.8, 6.4, and 7.1 keV), corresponding to their binding energies.

3.5. Analysis of the TEM images

The Fe_3O_4 nanostructures ($\Phi = 1$) were also characterized by TEM analysis (Figures 8a and 8b). The images reveal a high degree of dispersion achieved using the sample dispersion method. TEM images of the synthesized NPs crystals reveal the presence of spherical particles of uniform size. Well-crystallized morphology reliant on the applied fuel ratios was observed. The size distribution histogram obtained from the TEM measurements is presented in Figure 8c. The average particle size of the synthesized MNPs at $\Phi = 1$ is approximately 35.84 nm. This is a narrow size distribution. The particle size of Fe_3O_4, obtained by analyzing the TEM images, agrees well with the particle size obtained by analyzing the XRD profiles. The interplanar spacing (d), determined from the HRTEM images, indicate the (400) lattice plane (Figure 8d).

3.6. Analysis of the TG profiles

The TG/DSC profiles of the $Fe(NO_3)_3.9H_2O$ precursor is presented in Figure 9a. The first two endothermic peaks at 56 °C and 149 °C, with mass loss 75%, indicate the removal of water of crystallization and nitrogen oxides.

A third endothermic peak appears in the temperature range of 149–225 °C. The DSC curve presents an intense slope. Thermal decomposition occurs under conditions of such high temperatures (mass loss: 23%). This is accompanied by the elimination of nitrogen, NO_2, and water in the form of nitric acid (HNO_3) and iron oxide (Fe_2O_3) (Figure 9a). The mode of decomposition of ferric nitrate is represented by Equations 6 and 7 as follows [56].
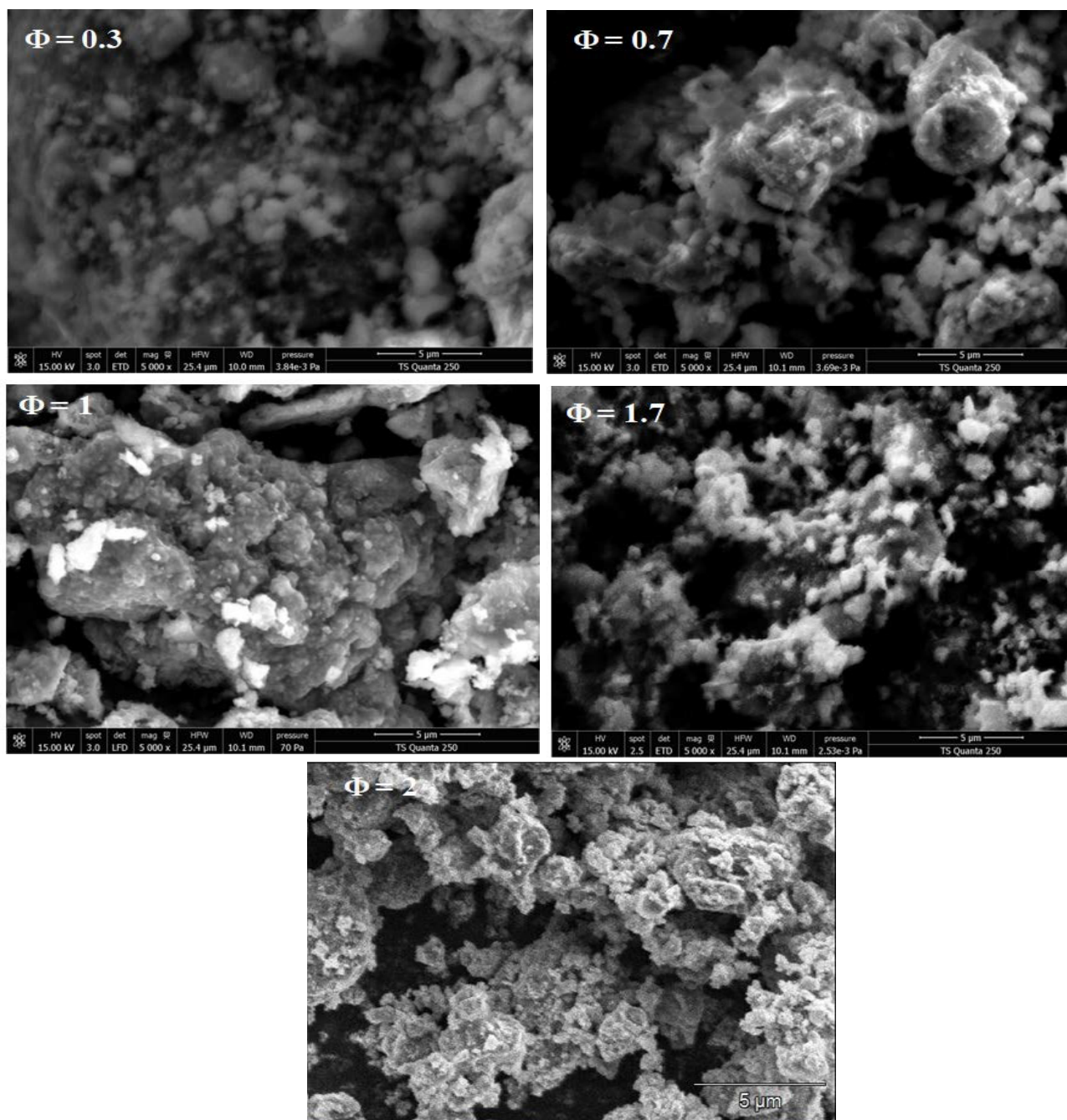
Figure 6. FESEM images of iron oxide nanoparticles at different starch to ferric nitrate ratios (Φ = 0.3, 0.7, 1, 1.7, and 2).

$$\text{Fe (NO}_3)_3.9\text{H}_2\text{O} \quad \rightarrow \quad \text{Fe (NO}_3)_3 + 9\text{H}_2\text{O}_{(g)} \tag{6}$$

$$4[\text{Fe (NO}_3)_3] \quad \rightarrow \quad 2\text{Fe}_2\text{O}_{3\,(s)} + 12\text{NO}_{2\,(g)} + 3\text{O}_{2(g)} \tag{7}$$

The combustion reactions occurring during the synthesis of iron oxide nanoparticles at fuel-lean conditions (Φ = 0.3) and fuel-rich conditions (Φ = 1.7) were analyzed using the TG-DSC technique. The temperature was raised to 700 °C from room temperature at a heating rate of 10 °C min^{-1} under an atmosphere of nitrogen (Figures 9b and 9c). The first stage (60 °C to 150 °C) of Figure 9b reveals the presence of two weak endothermic peaks that appear at 60 °C and 134 °C. The process
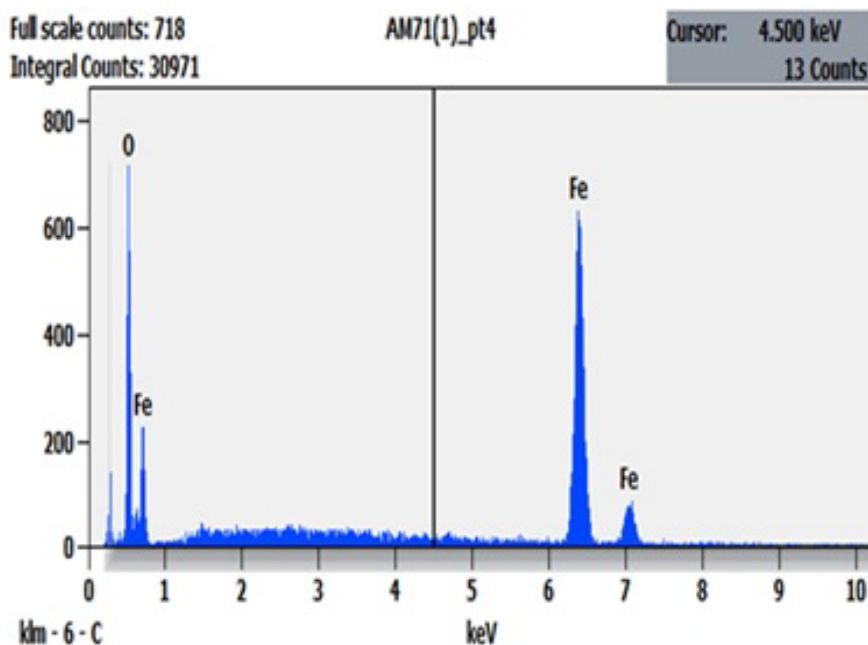
Figure 7. EDX spectral profile of the synthesized iron oxide nanoparticles.

occurring at this stage was accompanied by a weight loss of approximately 7%. Figure 9c reveals the presence of a broad endothermic peak in the region of 60–130 °C. The weight loss recorded at this stage was approximately 10%. The weight loss at this stage can be potentially attributed to the vaporization of residual water (from the precursor that was obtained after the drying process) and the decomposition of NH_4NO_3 (in the gelatinous mass) [30,31]. In the second temperature stage that ranges from 150 °C to 200 °C, a clear and sharp exothermic peak at approximately 200 °C was observed (Figure 9b). This stage was characterized by a high weight loss of 73% for dried gel under the lean fuel conditions ($\Phi = 0.3$). The weight loss decreased to 22% at approximately 200 °C Figure 8c, when the starch to ferric nitrate ratio increased under rich conditions ($\Phi = 1.7$). This temperature range (from 150 °C to 200 °C) is characteristic of the volatilization and the combustion reaction between ferric nitrate and starch in the gel with the release of H_2O, CO_2, and N_2 gases [57]. In the third and last stage (above 200 °C), as shown in Figure 9b, no loss in weight was observed, indicating the decrease in rates of oxidation and decomposition of organic residues with the increase in temperature and starch to ferric nitrate ratio. Figure 9c reveals a high exothermic peak at the temperature range between 300 °C and 450 °C, accompanied by a weight loss of 8%.

3.7. Porosity characterization
Figure 10a presents the N_2 adsorption-desorption isotherms of iron oxides synthesized at different starch to ferric nitrate ratios ($\Phi = 0.3, 0.7, 1, 1.7,$ and 2). The recorded isotherms exhibited types II and III isotherm hysteresis loops, indicating mesoporous structures. As shown in Figure 10b, the specific surface areas (SSAs) and the pore volume of the powders depend on the starch to ferric nitrate ratio (Φ). The SSA of the products under conditions of varying Φ ($\Phi = 0.3, 0.7, 1, 1.7,$ and 2) were found to be 16, 15, 4, 48, and 19 $m^2 g^{-1}$, respectively. The pore volumes of the products at different Φ values were 0.035, 0.027, 0.020, 0.058 and 0.028 $cm^3 g^{-1}$, respectively. The maximum SSA (48 $m^2 g^{-1}$) was recorded at $\Phi = 1.7$ (Figure 10b). This could be attributed to the rapid thermal decomposition process accompanied by the release of gases during the combustion reaction [57]. For $\Phi = 2$, the decrease in the specific surface area can be attributed to the sintering process and the growth of the particle size between iron nitrate and starch [34]. The pore size diameter of the combusted powder at different starch to ferric nitrate ratios ($\Phi = 0.3, 0.7, 1, 1.7$ and 2) were 14, 9, 37, 8, and 8 nm, respectively, indicating the mesoporous structure.

The BJH pore size distributions are illustrated in the inset of Figure 10c. The pore size distributions of the combusted powders at different starch to ferric nitrate ratios of $\Phi = 0.3, 0.7, 1, 1.7,$ and 2 were found to be 10, 4, 2.5, 3.5, and 4 nm, respectively. The pore size distribution at different ratios indicates a mesopore distribution.

3.8. UV-visible analysis
The optical properties of the synthesized iron oxides at different starch to ferric nitrate ratios ($\Phi = 0.3, 0.7, 1, 1.7,$ and 2) were investigated by the UV-vis DRS spectroscopy. It can be seen from Figure 11 that the absorbance spectra of the iron
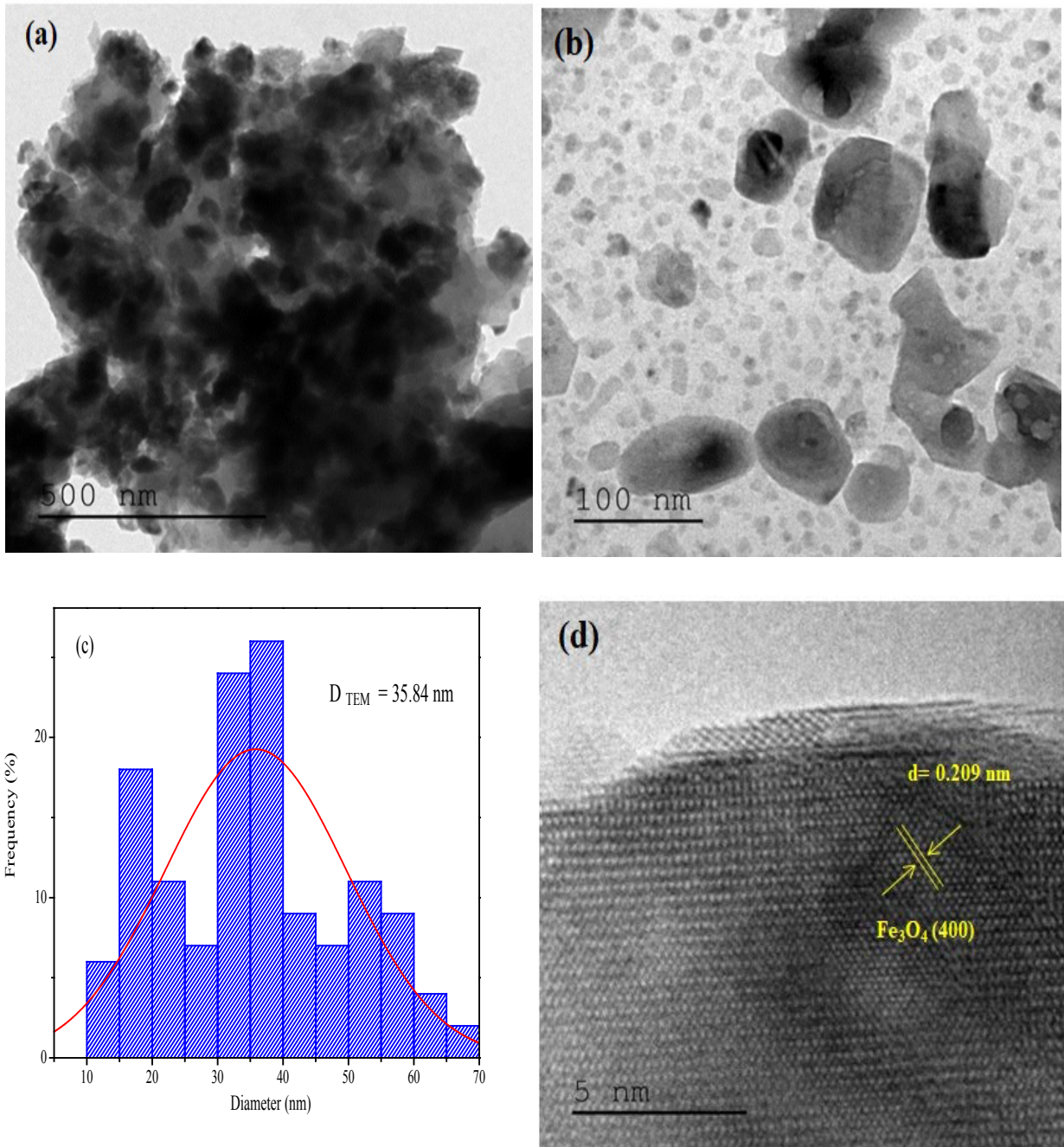
Figure 8. TEM images of magnetite nanoparticles (a,b), and size distribution histogram obtained from the TEM micrograph (c), and HRTEM micrograph with inter planar spacing of magnetite nanoparticles (d).

oxide nanoparticles are remarkably different with the variation of starch content. As shown in the Figure 12, the curve of α- Fe_2O_3 (Φ = 0.3 and 0.7) has a strong photo absorption in the visible region, while the curve of Fe_3O_4 (Φ = 1, 1.7 and 2) was very wide. The optical energy band gap was calculated by the Tauc's equation (Equation 8):

$$a(αhυ)^n = k (hυ − Eg)$$

(8)

where α and k are absorption coefficient and optical transition-dependent constant of the material under investigation, hυ is the photon energy, and Eg is the band gap energy of the material. The exponent "n" indicates the nature of optical transition in the semiconductor. Both hematite and magnetite have a direct band gap (n = 2). A plot of $(αhυ)^2$ versus hυ is shown
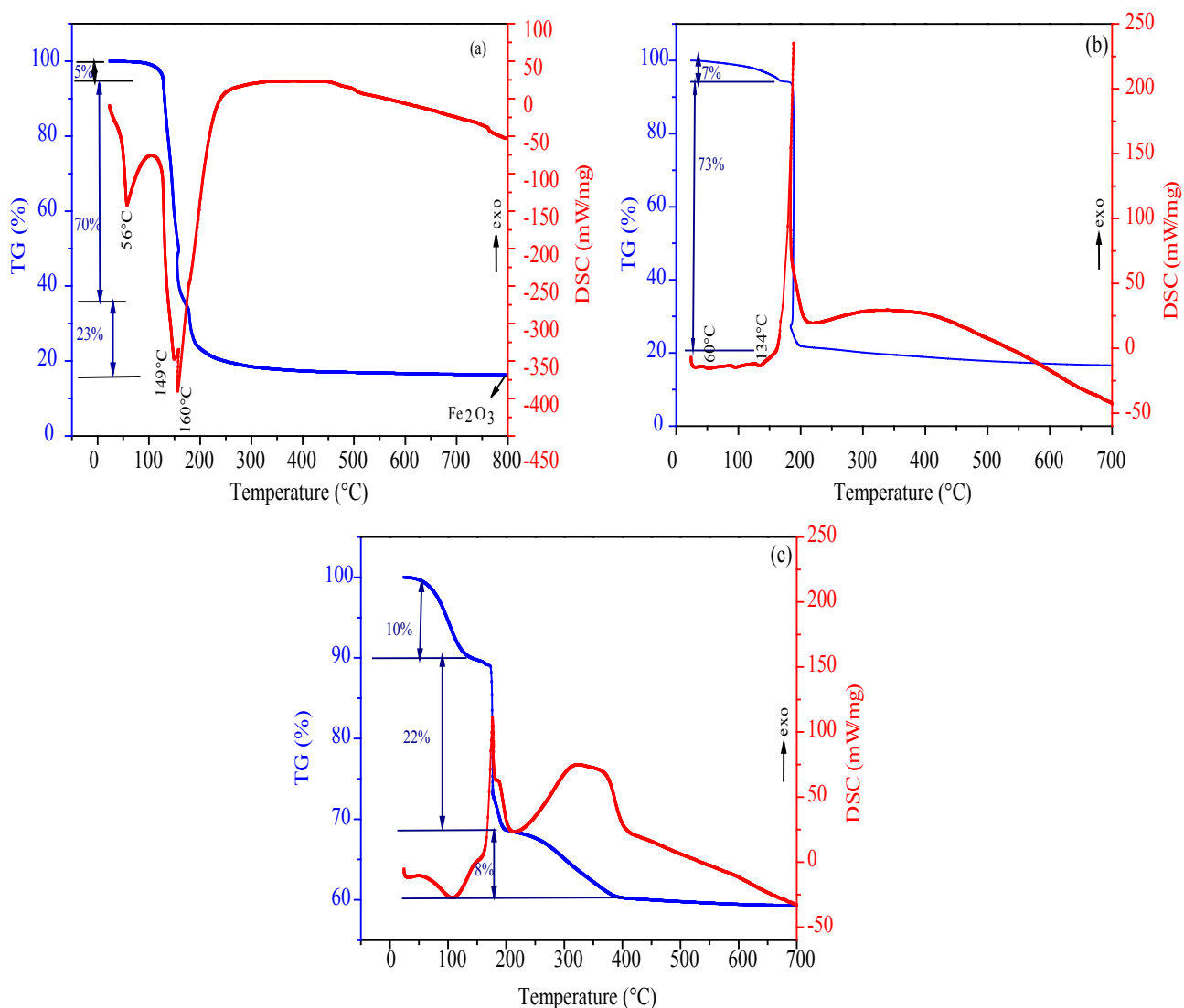
**Figure 9.** TG and DSC curves of Fe $(NO_3)_3 \cdot 9H_2O$ (a), and the dried gels at different starch to ferric nitrate ratios Φ = 0.3 (b) and Φ = 1.7 (c).

in Figure 12. The extrapolation of the linear portion of the $(\alpha.h\upsilon)^2$ versus the photon energy $(h\upsilon)$ axis provides the value of the optical band gaps Eg when $(\alpha.h\upsilon)^2$ is zero. The estimated optical band gaps energy of α-Fe_2O_3 at Φ = 0.3 and 0.7 are 1.99 and 1.82 which correspond with the reported value [58]. Table 2 presents the Band gap values of the prepared iron oxides at different starch to ferric nitrate ratios. This decrease of the value is due to the increase in the Φ ratio, the particle size increases that is responsible for decreasing the optical band gap [26]. The estimated optical band gaps energy of Fe_3O_4 at Φ = 1, 1.7 and 2 are 1.63, to 1.67 and 1.68, respectively (Table 2). The band gap energy increase with increasing of starch to ferric nitrate ratio. This increase of band gap energy is due to the decrease of the particle size of Fe_3O_4 nanoparticles [59]. From this observation, the difference in synthesized iron oxide nanoparticles can be attributed to the quantum size effect, with the size of the particles influencing their band gap energy [60].

3.9. Magnetic properties
Figure 13 reveals the magnetic hysteresis loop of the resultant iron oxide at different starch to ferric nitrate ratios Φ = 0.3, 0.7, 1, 1.7, and 2 recorded at room temperature with the maximum field of 70 KOe. The saturation magnetization (M_s), remanence (M_r) and coercivity (H_c) versus fuel ratio are listed in Table 3. It is remarkable that all the synthesized iron oxide nanoparticles are saturated at 70 KOe as well as the coercivity of the resultant iron oxide nanoparticles depend on the Φ ratios (Table 3). As shown in Figure 13, all the resultant iron oxide at different Φ ratios perform typical ferromagnetic
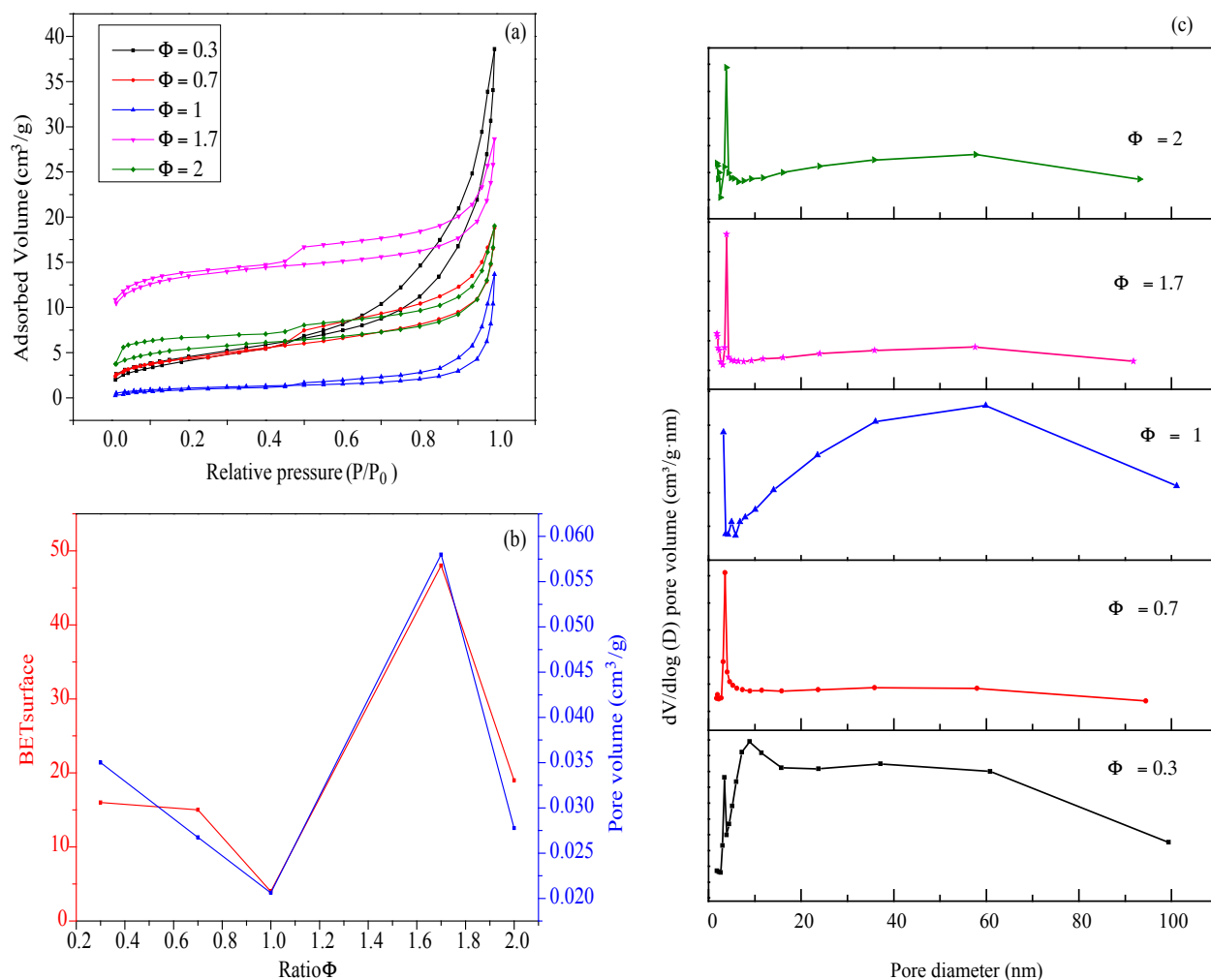
Figure 10. Nitrogen adsorption-desorption isotherms of the as-combusted powders at Φ = 0.3, Φ = 0.7, Φ = 1, Φ = 1.7, and Φ = 2 (a); and SBET and pore volume of iron oxide synthesized at different starch to ferric nitrate ratios (Φ) (b); and pore size distribution (c).

properties at room temperature (Table 3). It is important to note that Φ has a substantial impact on the magnetic properties of the resultant iron oxides nanoparticles revealing that M_s decreases as Φ ratios increase [57]. Consequently, the synthesized α-Fe_2O_3 at Φ = 0.3 and 0.7 present the lowest saturation magnetization 32.15 and 36.19 emu/g (Table 3). It may be attributed to the largest particle size with the highest surface area and small crystallite size of hematite compared with those of the magnetite nanoparticle [31,34,61]. Obviously, the saturation magnetization gets the highest value (60.36 emu/g) at Φ = 1 which is due to the formation of ferromagnetic Fe_3O_4 phase with high crystallinity and large crystallite size (35.84 nm) as previously confirmed by XRD and FTIR analysis, whereas the saturation magnetization decreased to 38.95 emu/g at the highest Φ ratios (1.7 and 2). This may be attributed to the increase of the residual carbon in the Fe_3O_4 nanoparticles that led to the lowest crystallinity as exhibited by the XRD (Figures 4 and 5).

4. Conclusion

Homogenous hematite and magnetite crystalline phases have been synthesized following a new single fuel combustion method. In this method, ferric nitrate has been used as the oxidant and starch has been used as the reducing organic fuel (in different molar ratios). Starch has been effectively used in the low-temperature fuel approach. The thermal analysis of the starch-based precursor revealed that the final decomposition temperature, morphology, and the crystallization process of iron oxides are influenced by the starch ratio. Therefore, the maximum amount of the oxidant relative to the amount of fuel for Φ < 1 results in the formation of the maximum amounts of gases that form α-Fe_2O_3 as the main phase and Rietveld structure refinement analysis confirmed the formation of single Fe_3O_4 at Φ = 1. The α-Fe_2O_3 phase is reduced to Fe_3O_4 when
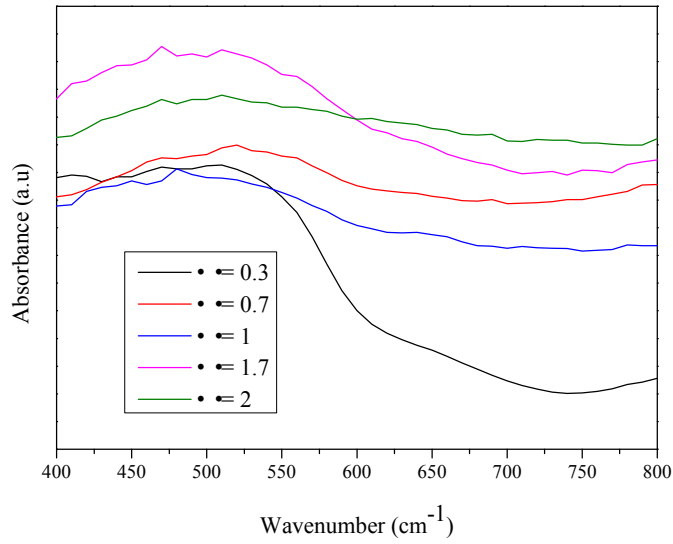
Figure 11. UV-vis DRS spectra of the resultant oxides at different starch to ferric nitrate ratios (Φ = 0.3, 0.7, 1, 1.7, and 2).
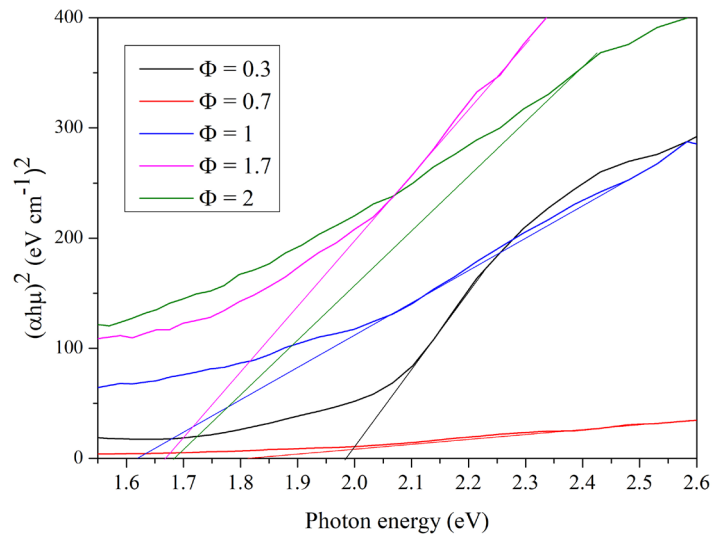
Figure 12. $(\alpha h\mu)^2$ as function of photon energy $h\mu$ for determining the optical bandgap of iron oxide nanoparticles at different starch to ferric nitrate ratios (Φ = 0.3, 0.7, 1, 1.7, and 2).

Table 2. Band gap of the resultant iron oxide at different starch to ferric nitrate ratios Φ.

Fuel ratio Φ	Band gap energy (eV)
0.3	1.98
0.7	1.82
1	1.63
1.7	1.67
2	1.68
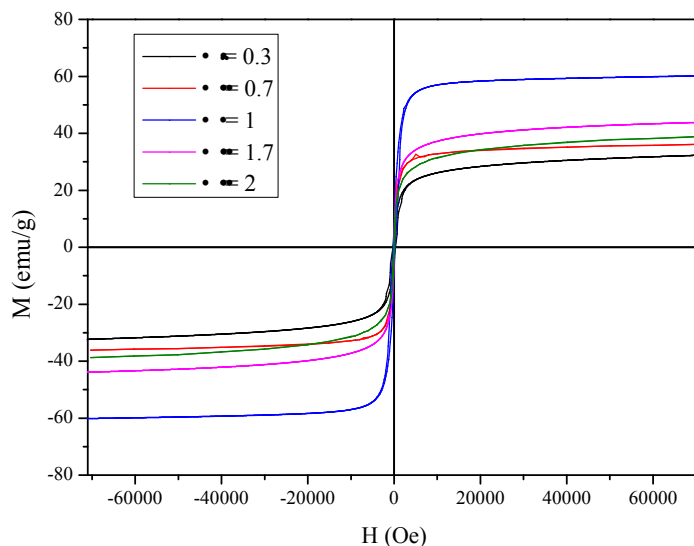
Figure 13. Magnetic hysteresis loop of the resultant iron oxide at different starch to ferric nitrate ratios Φ = 0.3, 0.7, 1, 1.7, and 2.

Table 3. VSM magnetic parameters from major loop.

Fuel ratio Φ	Ms (emu/g)	Mr (emu/g)	Hc (Oe)
0.3	32.15	4.18	273.4
0.7	36.19	6.73	142.90
1	60.36	8.48	263.66
1.7	44.14	5.10	145.20
2	38.95	4.12	105.21

the reducing gas (CO) is present under conditions of high fuel content ($\Phi \geq 1$). The porosity characterization indicated mesoporous structures of α-Fe_2O_3 and Fe_3O_4 phase with the highest specific surface area of 48 m^2 g^{-1} at Φ = 1.7. The magnetic properties of Fe_3O_4 powders synthesized at Φ = 1 showed the highest saturation magnetization of 60.36 emu/g with high crystallinity. The proposed simple, fast, cheap, and environmentally friendly synthetic route can be considered as an alternative way to prepare pure hematite and magnetite in high quantity as the MNPs find their applications in various fields (e.g., biomedical field).

Conflict of interest
No potential conflict of interest was reported by the authors.

References

1. Salata OV. Applications of nanoparticles in biology and medicine. Journal of Nanobiotechnology 2004; 2 (1): 3. doi: 10.1186/1477-3155-2-3

2. Laurent S, Forge D, Port M, Roch A, Robic C et al. Magnetic iron oxide nanoparticles: synthesis, stabilization, vectorization, physicochemical characterizations, and biological applications. Chemical Reviews 2008; 108 (6): 2064-2110. doi: 10.1021/cr068445e

3. Ahmed MK, Zayed MA, El-dek SI, AbdelHady M, El Sherbiny DH et al. Nanofibrous ε-polycaprolactone scaffolds containing Ag-doped magnetite nanoparticles: Physicochemical characterization and biological testing for wound dressing applications in vitro and in vivo. Bioactive Materials 2021; 6 (7): 2070-2088. doi: 10.1016/j.bioactmat.2020.12.026

4. Narayanan KB, Han SS. One-pot green synthesis of hematite (α-Fe$_2$O$_3$) nanoparticles by ultrasonic irradiation and their in vitro cytotoxicity on human keratinocytes CRL-2310 Journal of Cluster Science 2016; 27: 1763–1775. doi: 10.1007/s10876-016-1040-9

5. Ghartavol RV, Borojeni ABM, Ghartavol ZV, Aiyelabegan HT, Jaafari MR et al. Toxicity assessment of superparamagnetic iron oxide nanoparticles in different tissues. Artificial Cells, Nanomedicine, and Biotechnology 2019; 48 (1): 443–451 10. doi: 1080/21691401.2019.1709855

6. Zhao S, Lee S. Biomaterial-modified magnetic nanoparticles γ-Fe$_2$O$_3$, Fe$_3$O$_4$ Used to improve the efficiency of hyperthermia of tumors in HepG2 Model. Applied Sciences 2021; 11 (5): 2017. doi: 10.3390/app11052017

7. Reza Yasemian A, Almasi Kashi M, Ramazani A. Surfactant-free synthesis and magnetic hyperthermia investigation of iron oxide (FeO) nanoparticles at different reaction temperatures. Materials Chemistry and Physics 2019; 230: 9-16. doi: 10.1016/j.matchemphys.2019.03.032

8. Keshk SMAS, El-Zahhar AA, Alsulami QA, Jaremko M, Bondock S et al. Synthesis, characterization and ampyrone drug release behavior of magnetite nanoparticle/2,3-dialdehyde cellulose6-phosphate composite. Cellulose 2020; 27 (13): 1603-1618. doi: 10.1007/s10570-019-02887-y

9. Bleul R, Bak Ai, Freese C, Paysen H, Kosch O et al. Continuously manufactured single-core iron oxide nanoparticles for cancer theranostics as valuable contribution in translational research. Nanoscale Advances 2020; 2: 4510-4521. doi: 10.1039/D0NA00343C

10. Bakenecker AC, Ahlborg M, Debbeler C, Kaethner C, Buzug TM et al. Magnetic particle imaging in vascular medicine. De Gruyter 2018; 3 (3): 179-192. doi: 10.1515/iss-2018-2026

11. Akram N, Ma W, Guo J, Guo Y, Yansong Z et al. Ynergistic catalysis of Fe$_3$O$_4$/CuO bimetallic catalyst derived from Prussian blue analogues for the efficient decomposition of various organic pollutants. Chemical Physics 2021; 45: 110974. doi: 10.1016/j.chemphys.2020.110974

12. Nasrollahzadeh M, Issaabadi Z, Sajadi SM. Green synthesis of Pd/Fe3O4 nanocomposite using Hibiscus tiliaceus L. extract and its application for reductive catalysis of Cr(VI) and nitro compounds. Separation and Purification Technology 2018; 197: 253-260. doi: 10.1016/j.seppur.2018.01.010

13. Liu Y, Wei R, Ding W, Wang X, Song W et al. Porous Fe$_3$O$_4$ thin films by pulsed laser assisted chemical solution deposition at room temperature. Applied Surface Science2019; 478: 408-411. doi: 10.1016/j.apsusc.2019.01.282

14. Ali A, Zafar H, Zia M, Ul Haq I, Phull AR et al. Synthesis, characterization, applications, and challenges of iron oxide nanoparticles. Nanotechnology, Science and Applications 2016; 9: 49-67. doi: 10.2147/NSA.S99986

15. Sun SN, Wei C, Zhu ZZ, Hou YL, Venkatraman SS et al. Magnetic iron oxide nanoparticles: Synthesis and surface coating techniques for biomedical applications. Chinese Physics B 2014; 23 (3): 037503. doi: 10.1088/1674-1056/23/3/037503

16. Nisticò R. A synthetic guide toward the tailored production of magnetic iron oxide nanoparticles. Boletín de la Sociedad Española de Cerámica y Vidrio 2021; 60: 29-40.

17. Vargas G, Cypriano J,Correa T, Leao P, Bazylinski DA et al. Applications of magnetotactic bacteria,magnetosomes and magnetosome crystals in biotechnology and nanotechnology: mini-review. Molecules (2018); 23: 2438. doi: 10.3390/molecules23102438

18. Jesus ACB, Jesus JR, Lima RJS, Moura KO, Meneses JMA et al. Synthesis and magnetic interaction on concentrated Fe$_3$O$_4$ nanoparticles obtained by the co-precipitation and hydrothermal chemical methods. Ceramics International 2020; 48 (8): 11149-11153. doi: 10.1016/j.ceramint.2020.01.135

19. Besenhard MO, LaGrow AP, Hodzice H, Kriechbaum M, Panariello L et al. Co-precipitation synthesis of stable iron oxide nanoparticles with NaOH: New insights and continuous production via flow chemistry. Chemical Engineering Journal 2020; 399: 125740. doi: 10.1016/j.cej.2020.125740

20. Lassoued A, Lassoued MS, Dkhil B, Ammar S, Gadri A. Photocatalytic degradation of methylene blue dye by iron oxide (α-Fe$_2$O$_3$) nanoparticles under visible irradiation. Journal of Materials Science: Materials in Electronics 2018; 29 (10): 8142-8152. doi: 10.1007/s10854-018-8819-4

21. Takai ZI, Mustafa MK, Asman S, Sekak KA. Preparation and characterization of magnetite (Fe$_3$O$_4$) nanoparticles By sol-gel method. International Journal of Nanoelectronics and Materials 2019; 12: 37-46.

22. Rakibuddin MD, Kim H. Sol-gel derived Fe$_3$O$_4$ quantum dot decorated silica composites for effective removal of arsenic (III) from water. Materials Chemistry and Physics 2020; 240: 122245. doi: 10.1016/j.matchemphys.2019.122245

23. Boumaza S, Kabir H, Gharbia I, Belhadi A, Trari M. Preparation and photocatalytic H2-production on α-Fe$_2$O$_3$ prepared by sol-gel. International Journal of Hydrogen Energy 2018; 43 (6): 3424-3430. doi: 10.1016/j.ijhydene.2017.07.227

24. Cheng L, Ruan W, Zou B, Liu Y, Wang Y. Chemical template-assisted synthesis of monodisperse rattle-type Fe$_3$O$_4$@C hollow microspheres as drug carrier. Acta Biomaterialia 2017; 58: 432-441. doi: 10.1016/j.actbio.2017.06.007

25. Azizabadi O, Akbarzadeh F, Danshina S, Chauhan NPS, Sargazi G. An efficient ultrasonic assisted reverse micelle synthesis route for Fe_3O_4@Cu-MOF/core-shell nanostructures and its antibacterial activities. Journal of Solid State Chemistry 2021; 294: 121897. doi: 10.1016/j.jssc.2020.121897

26. Lassoued A, Lassoued MS, Dkhil B, Ammar S, Gadri A. Synthesis, photoluminescence and Magnetic properties of iron oxide (α-Fe_2O_3) nanoparticles through precipitation or hydrothermal methods. Physica E: Low-dimensional Systems and Nanostructures 2018; 101: 212-219. doi: 10.1016/j.physe.2018.04.009

27. Fotukian SM, Barati A, Soleymani M, Alizadeh AM. Solvothermal synthesis of $CuFe_2O_4$ and Fe_3O_4 nanoparticles with high heating efficiency for magnetic hyperthermia application. Journal of Alloys and Compounds 2020; 816: 152548. doi: 10.1016/j.jallcom.2019.152548

28. Balachandramohan J, Anandar S, Sivasankar T. A simple approach for the sonochemical synthesis of Fe_3O_4-guargum nanocomposite and its catalytic reduction of p-nitroaniline. Ultrasonics Sonochemistry 2018; 40: 1-10. doi: 10.1016/j.ultsonch.2017.06.012

29. Yadav RS, Kuřitka I, Vilcakova J, Havlica J, Kalina L et al. Sonochemical synthesis of Gd^{3+} doped $CoFe_2O_4$ spinel ferrite nanoparticles and its physical properties. Ultrasonics Sonochemistry 2018; 40: 773–783. doi: 10.1016/j.ultsonch.2017.08.024

30. Zhang X, Han D, Hua Z, Yang S. Porous Fe_3O_4 and gamma-Fe_2O_3 foams synthesized in air by sol-gel autocombustion. Journal of Alloys and Compounds 2016 ; 684: 120-124. doi: 10.1016/j.jallcom.2016.05.159

31. Wang X, Qin M, Fang F, Jia B, Wu H et al. Effect of glycine on one-step solution combustion synthesis of magnetite nanoparticles. Journal of Alloys and Compounds 2017; 719 (5): 288-295. doi: 10.1016/j.jallcom.2017.05.187

32. Belekar R M. Structural and electrical studies of nanocrystalline Fe_2O_3 prepared by microwave assisted solution combustion method with mixed fuel approach. Journal of Physical Sciences 2018; 23: 189-199.

33. Rouhani AR, Esmaeil-Khanian AH, Davar F, Hasani S. The effect of agarose content on the morphology, phase evolution, and magnetic properties of $CoFe_2O_4$ nanoparticles prepared by sol-gel autocombustion method. International Journal of Applied Ceramic Technology 2017; 15 (3): 758-765. doi: 10.1111/ijac.12832

34. Hadadian S, Masoudpanah SM, Alamolhoda S. Solution combustion synthesis of Fe_3O_4 powders using mixture of CTAB and citric acid fuels. Journal of Superconductivity and Novel Magnetism 2019; 32: 353–360. doi: 10.1007/s10948-018-4685-9

35. Karimzadeh I, Aghazadeh M, Doroudi T, Reza Ganjali M, Hossein Kolivand P. Effective preparation, characterization and in situ surface coating of superparamagnetic Fe_3O_4 nanoparticles with polyethyleneimine through cathodic electrochemical deposition (CED). Current Nanoscience 2017; 13 (2); 167-174. doi: 10.2174/1573413713666161129160640

36. Salima P, Norouzi O , Pourhosseini SEM. Two-step synthesis of nanohusk Fe_3O_4 embedded in 3D network pyrolytic marine biochar for a new generation of anode materials for Lithium-Ion batteries. Journal of Alloys and Compounds 2019; 786 (25): 930-937. doi: 10.1016/j.jallcom.2019.02.048

37. Patil KC, Hegde MS, Rattan T, Aruna ST. Chemistry of Nanocrystalline Oxide Materials, Combustion Synthesis, Properties and Applications. New Jersey, États-Unis: World Scientific, 2008.

38. Šutka A, Lagzdina S, Käämbre T, Pärna R, Kisand V et al. Study of the structural phase transformation of iron oxide nanoparticles from an Fe^{2+} ion source by precipitation under various synthesis parameters and temperatures. Materials Chemistry and Physics 2015; 149: 473-479. doi: 10.1016/j.matchemphys.2014.10.048

39. Hashemi S M, Hasani S, Ardakani K J, Davar F. The effect of simultaneous addition of ethylene glycol and agarose on the structural and magnetic properties of $CoFe_2O_4$ nanoparticles prepared by the sol-gel auto-combustion method. Journal of Magnetism and Magnetic Materials 2019; 492 (15): 165714. doi: 10.1016/j.jmmm.2019.165714

40. Imanipour P, Hasani S, Seifoddini A, Farnia A, Karimabadi F et al.The possibility of vanadium substitution on Co lattice sites in $CoFe_2O_4$ synthesized by sol–gel autocombustion method. Journal of Sol-Gel Science and Technology 2020; 20: 167: 157–167. doi: 10.1007/s10971-020-05316-w

41. Visinescu D, Paraschiv C, Ianculescu A, Jurca B, Vasile B et al. The environmentally benign synthesis of nanosized CoxZn1−xAl2O4 blue pigments. Dyes and Pigments 2010; 87 (2): 125-131. doi: 10.1016/j.dyepig.2010.03.006

42. Keshk SMAS, El-Zahhar AA, Haija MA, Bondock S. Synthesis of a magnetic nanoparticles/dialdehyde starch-based composite film for food packaging. Starch - Stärke 2019; 71: 1800035. doi: 10.1002/star.201800035

43. Afshari M, Isfahani A R, Hasani S, Davar F, ArdakaniK J. Effect of apple cider vinegar agent on the microstructure, phase evolution, and magnetic properties of $CoFe_2O_4$ magnetic nanoparticles. International Journal of Applied Ceramic Technology 2019; 16 (4): 1612-1621. doi: 10.1111/ijac.13224.

44. Ben Bettaïeb N, Jerbi MT, Ghorbel D. Gamma radiation influences pasting, thermal and structural properties of corn starch. Radiation Physics and Chemistry 2014; 103: 1-8. doi: 10.1016/j.radphyschem.2014.05.011

45. Varma A, Mukasyan AS, Rogachev AS, Manukyan KV. Solution combustion synthesis of nanoscale materials. Chemical Reviews 2016; 116 (23): 14493-14586. doi: 10.1021/acs.chemrev.6b00279

46. Lee JH, Hun JA, Lim ST. Effect of pH on aqueous structure of maize starches analyzed by HPSEC-MALLS-RI system. Food Hydrocolloids 2009; 23: 1935. doi: 10.1016/j.foodhyd.2008.12.007

47. Danks AE, Hall SR, Schnepp Z. The evolution of 'sol–gel' chemistry as a technique for materials synthesis. Materials Horizons 2016; 3: 91-112. doi: 10.1039/c5mh00260e

48. Holzwarth U, Gibson N. The Scherrer equation versus the 'Debye-Scherrer equation'. Nature Nanotechnology 2011; 6 (9): 534-534. doi: 10.1038/nnano.2011.145

49. Stodt MFB, Gonchikzhapov M, Kasper T, Fritsching U, Kiefer J. Chemistry of iron nitrate-based precursor solutions for spray-flame synthesis. Physical Chemistry Chemical Physics 2019; 21 (44): 24793-24801. doi: 10.1039/C9CP05007H

50. Vargas MA, Diosa JE, Mosquera E. Data on study of hematite nanoparticles obtained from Iron(III) oxide by the Pechini method. Data Brief 2019; 25: 104183. doi: 10.1016/j.dib.2019.104183

51. Istratie R, Stoia M, Păcurariu C, Locovei C. Single and simultaneous adsorption of methyl orange and phenol onto magnetic iron oxide/carbon nanocomposites. Arabian Journal of Chemistry 2019; 12 (8): 3704-3722. doi: 10.1016/j.arabjc.2015.12.012

52. Hussain M, Khan R, Zulfiqar S, Khan T, Khan G et al. Dielectric and magnetic properties of cobalt doped γ-Fe_2O_3 nanoparticles. Journal of Materials Science: Materials in Electronics 2019; 30: 13698–13707. doi: 10.1007/s10854-019-01747-6

53. Kannana PK, Saraswathi R. An impedimetric ammonia sensor based on nanostructured α-Fe_2O_3. Journal of Materials Chemistry A 2014; 2: 394-401. doi: 10.1039/C3TA13553E

54. Hu P, Zhang S, Wang H, Pan Da, Tian J et al. Heat treatment effects on Fe_3O_4 nanoparticles structure and magnetic properties prepared by carbothermal reduction. Journal of Alloys and Compounds 2011; 509 (5): 2316-2319. doi: 10.1016/j.jallcom.2010.10.211

55. Toniolo J, Takimi AS, Andrade MJ, Bonadiman R, Bergmann CP. Synthesis by the solution combustion process and magnetic properties of iron oxide (Fe_3O_4 and α-Fe_2O_3) particles. Journal of Materials Science 2007; 42 (13): 4785-4791. doi: 10.1007/s10853-006-0763-7

56. Shaheen WM. Thermal behaviour of pure and binary $Fe(NO_3)_3$·$9H_2O$ and $(NH_4)_6Mo_7O_{24}$·4H2O systems. Materials Science & Engineering A 2007; 445 (2007): 113-121. doi: 10.1016/j.msea.2006.09.007

57. Fathi H, Masoudpanah SM, Alamolhoda S, Parnianfar H. Effect of fuel type on the microstructure and magnetic properties of solution combusted Fe_3O_4 powders. Ceramics International 2017; 43 (10): 7448-7453. doi: 10.1016/j.ceramint.2017.03.017

58. Cao Z, Qin M, Jia B, Gu Y, Chen P et al. One pot solution combustion synthesis of highly mesoporous hematite for photocatalysis. Ceramics International 2015; 41 (2): 2806-2812. doi: 10.1016/j.ceramint.2014.10.100

59. Reyes Villegas VA, De León Ramírez JI, Hernandez Guevara I, Perez Sicairos S, Hurtado Ayala LA et al. Synthesis and characterization of magnetite nanoparticles for photocatalysis of nitrobenzene. Journal of Saudi Chemical Society 2020; 24 (2): 223-235. doi: 10.1016/j.jscs.2019.12.004

60. El-Diasty F, El-Sayed HM, El-Hosiny FI, Ismail MIM. Complex susceptibility analysis of magneto-fluids: Optical band gap and surface studies on the nanomagnetite-based particles. Current Opinion in Solid State and Materials Science 2009; 13 (1-2): 28-34. doi: 10.1016/j.cossms.2008.09.002

61. Ahmadzadeh M, Romero C, McCloy J. Magnetic analysis of commercial hematite, magnetite, and their mixtures. AIP ADVANCES 2018; 8 (5): 2158-3226. doi: 10.1063/1.5006474